JACS
JOURNAL OF THE AMERICAN CHEMICAL SOCIETY
Article
pubs.acs.org/JACS

Pressure Induced Phase Transitions and Metallization of a Neutral Radical Conductor

Joanne W. L. Wong,[†] Aaron Mailman,[†] Kristina Lekin,[†] Stephen M. Winter,[†] Wenjun Yong,[‡] Jianbao Zhao,[§] Subrahmanyam V. Garimella,[§] John S. Tse,[§] Richard A. Secco,[‡] Serge Desgreniers,[#] Yasuo Ohishi,[⊥] Ferenc Borondics,[∥] and Richard T. Oakley*[,†]

[†]Department of Chemistry, University of Waterloo, Waterloo, Ontario N2L 3G1, Canada
[‡]Department of Earth Sciences, University of Western Ontario, London, Ontario N6A 5B7, Canada
[§]Department of Physics and Engineering Physics, University of Saskatchewan, Saskatoon, Saskatchewan S7N 5E2, Canada
[#]Department of Physics, University of Ottawa, Ottawa, Ontario K1N 6N5, Canada
[⊥]Materials Science Division, Japan Synchrotron Radiation Research Institute (JASRI), SPring-8, Sayo, Hyogo 679-5198, Japan
[∥]Canadian Light Source, Saskatoon, Saskatchewan S7N 5B3, Canada

Supporting Information

ABSTRACT: The crystal structure and charge transport properties of the prototypal oxobenzene-bridged 1,2,3-bisdithiazolyl radical conductor **3a** are strongly dependent on pressure. Compression of the as-crystallized α-phase, space group *Fdd*2, to 3−4 GPa leads to its conversion into a second or β-phase, in which *F*-centering is lost. The space group symmetry is lowered to $Pbn2_1$, and there is concomitant halving of the *a* and *b* axes. A third or γ-phase, also space group $Pbn2_1$, is generated by further compression to 8 GPa. The changes in packing that accompany both phase transitions are associated with an "ironing out" of the ruffled ribbon-like architecture of the α-phase, so that consecutive radicals along the ribbons are rendered more nearly coplanar. In the β-phase the planar ribbons are propagated along the *b*-glides, while in the γ-phase they follow the *n*-glides. At ambient pressure **3a** is a Mott insulator, displaying high but activated conductivity, with σ(300 K) = 6×10^{-3} S cm^{-1} and E_{act} = 0.16 eV. With compression beyond 4 GPa, its conductivity is increased by 3 orders of magnitude, and the thermal activation energy is reduced to zero, heralding the formation of a metallic state. High pressure infrared absorption and reflectivity measurements are consistent with closure of the Mott−Hubbard gap near 4−5 GPa. The results are discussed in the light of DFT calculations on the molecular and band electronic structure of **3a**. The presence of a low-lying LUMO in **3a** gives rise to high electron affinity which, in turn, creates an electronically much softer radical with a low onsite Coulomb potential *U*. In addition, considerable crystal orbital (SOMO/LUMO) mixing occurs upon pressurization, so that a metallic state is readily achieved at relatively low applied pressure.

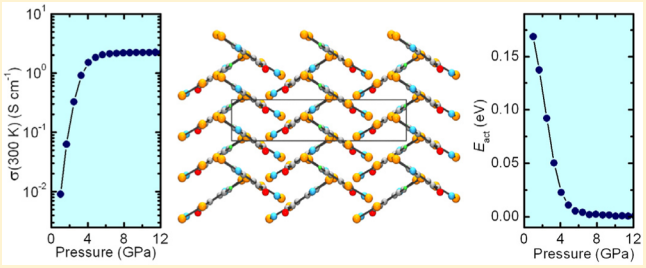

INTRODUCTION

Over a century has passed since McCoy and Moore suggested that an "aggregate of radicals would be a body with metallic properties".[1] While appealing in its simplicity, the idea that the unpaired electron present in a molecular radical could serve as a carrier of charge, just like the valence electron in a metallic element like sodium, has serious shortcomings. First, in an ordered array of radicals, as in a crystal, there is a large onsite Coulomb repulsion energy *U* associated with charge transport. Second, in all organic conductors, including charge-transfer salts,[2] intermolecular orbital overlap and the resulting electronic bandwidth *W* are notoriously small, so that site-to-site hopping of electrons is restricted. This large *U*/*W* ratio ensures that in most radical-based materials the unpaired electrons are isolated, and the system as a whole is trapped in a Mott insulating state.[3] The localized spins may nonetheless experience intermolecular magnetic exchange interactions, and extensive work[4] on the magnetic properties of light heteroatom (N/O) radicals, such as nitroxyls, verdazyls, and triazinyls, has demonstrated that ferromagnetic ordering can be achieved, albeit at low temperature (< 5 K).[5]

The electronic criteria to improve charge transport are conceptually simple but practically demanding. Radicals must be designed such that charge correlation is reduced and intermolecular overlap enhanced. Within the framework of the Hubbard model[6] a metallic state based on a half-filled energy band (an $f = {}^1/_2$ system) requires that the electronic bandwidth be sufficient to offset charge correlation, that is $W > U$.[7] Haddon was the first to recognize and address this challenge,[8]

Received: October 29, 2013
Published: January 8, 2014

   dx.doi.org/10.1021/ja411057x | *J. Am. Chem. Soc.* 2014, 136, 1070−1081

and in the mid-1970's he proposed the use of odd-alternant hydrocarbons based on the phenalenyl (PLY) framework, as their highly delocalized spin distributions and consequent low charge fluctuation energies make them appealing candidates for single component organic metals. Many variations on the original PLY template have been pursued, exploring substituent effects, more complex polycyclic frameworks, and the use of mixed valence spiro-conjugated PLYs.[9,10] While some high conductivities have been reported, the conductivity remains activated in all cases; a metallic state has yet to be observed.

An alternative approach to radical-based materials where $W > U$ involves the use of heavy heteroatoms.[11] As in the world of charge-transfer conductors, where the presence of sulfur and its heavier congeners imparts both softness (a lower U) and increased orbital overlap (a larger W) to donors such as tetrathiafulvalene (TTF)[12] and its derivatives,[2a,13] so too does the incorporation of sulfur and selenium into neutral radicals.[14] However, the incorporation of heavy heteroatoms into organic radicals comes at a cost, as the propensity for dimerization, with a consequent quenching of spin and charge carriers, is dramatically increased. As a result, early attempts to generate superimposed radical π-stacks using simple monocyclic thiazyl radicals afforded diamagnetic, Peierls distorted[15] structures with insulating or only weakly semiconducting ground states.[16,17] Improvements in conductivity could be induced by p-type doping,[18] which lowered U by changing the degree of band filling, but within the confines of the half-filled band ($f = {}^1/_2$) paradigm the challenge has been to reduce U, increase W, and prevent dimerization by molecular modification of the radical itself.

Resonance stabilized N-alkyl pyridine-bridged bisdithiazolyls **1** (Chart 1) were developed with these objectives in mind.[19] As

Chart 1

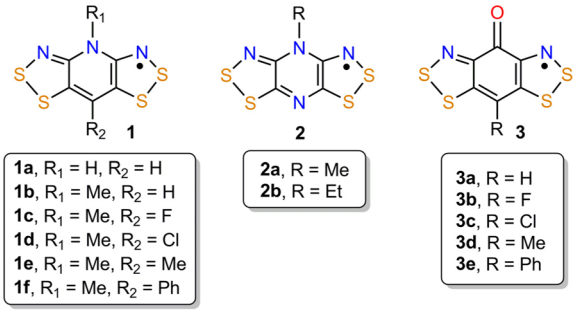

a result of spin delocalization across the entire tricyclic framework of these radicals, their gas-phase disproportionation energies ΔH_{disp} and electrochemical cell potentials E_{cell},[20] which provide indirect measures of U, are substantially lower than those of simple monocyclic thiazyl radicals.[21] Variations in the exocyclic groups R_1 and R_2 allow for fine-tuning of solid-state structures and hence intermolecular magnetic and electronic interactions.[22] Selenium incorporation into **1** can also be effected,[23] a modification which not only improves intermolecular overlap and conductivity but also increases magnetic exchange and magnetic anisotropy.[24] From these "heavy atom" building blocks bulk ferromagnets with ordering (Curie) temperatures T_C of 17 K and coercive fields H_c as high as 1600 Oe (at 2 K) have been developed.[25] However, regardless of the nature of the beltline ligands R_1 and R_2, most radicals of this type adopt herringbone packing patterns in the solid state, as illustrated in Figure 1a. While this arrangement helps

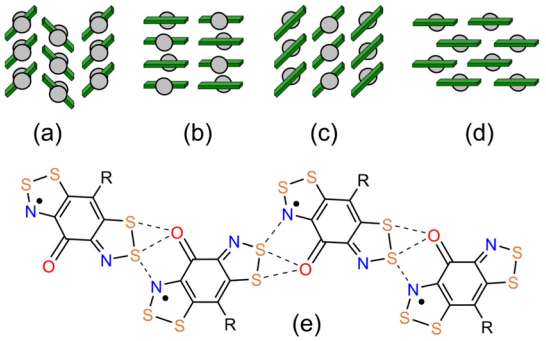

Figure 1. Packing motifs found in **1**, **2**, and **3**: (a) herringbone π-stacks, (b) alternating head-over-tail π-stacks, (c) slipped ribbon π-stacks, (d) brick wall π-stacks, and (e) ribbon-like arrays of radicals **3**.

suppress dimerization, it also compromises intra- and interstack overlap and hence charge transport. Isoelectronic replacement of the basal carbon by nitrogen, as in the N-alkylated pyrazine-bridged radicals **2** (Chart 1) removes the steric congestion created by the R_2 ligand but renders the radical more vulnerable to dimerization, as found in the ethyl derivative **2b**.[26] The methyl compound **2a**, however, crystallizes in evenly spaced, head-over-tail π-stacked arrays (Figure 1b), which affords improved conductivity.[27] Below 120 K, however, this structure also collapses into diamagnetic dimers.

As a continuation of efforts to break away from the herringbone packing found for **1**, while at the same time avoiding the dimerization problems encountered in **2**, we have recently explored the effects on structure and property of the formally isoelectronic replacement of the N-alkyl group of **1** with a carbonyl moiety, as in the oxobenzene-bridged radicals **3a**–**3e** (Chart 1).[28] Common to all these materials is the dramatic change in solid-state packing occasioned by the seemingly innocuous NR_1/CO exchange. In contrast to the N-R_1 group in **1**, whose structural role is largely to buffer intermolecular interactions, the polar C═O group serves as a supramolecular synthon,[29] forming strong, primarily electrostatic intermolecular C═O···S′ contacts which, when combined with more well-known N···S′ interactions,[30] generate planar ribbon-like arrays of radicals, as illustrated in Figure 1e. These molecular ribbons constitute the basic building blocks found in these materials, but within the family **3a**–**3e**, there are differences in the way the ribbons are arranged in the lattice. In the case of **3e** (R = Ph)[28a] the ribbons are overlaid to produce a highly one-dimensional (1D) head-over-tail arrangement (Figure 1b) of radicals, as found in **2a**, although, in contrast to the latter,[27] low-temperature dimerization does not occur. A quasi-1D stacking arrangement is also found in **3d** (R = Me).[28b] By contrast, in **3c**·MeCN (an acetonitrile solvate) the ribbons are packed in slipped π-stacks arrays (Figure 1c), a motif which affords a more 2D electronic structure,[28c] while in **3b** (R = F) the rigorously coplanar ribbons are layered into a "brick wall" packing pattern (Figure 1d), to produce a perfectly 2D electronic structure which metallizes on compression to just 3 GPa.[28d,31]

The prototypal radical **3a** (R = H) has one structural feature not present in other members of the set.[28e] The basal C–H unit serves as a supramolecular structure-maker, engaging in edge-to-face or tilted-T (donor–acceptor) contacts with neighboring arene carbons. These interactions cause a ruffling of the otherwise coplanar ribbon-like arrays of radicals, and this compromises electronic dimensionality and conductivity. We

dx.doi.org/10.1021/ja411057x | J. Am. Chem. Soc. 2014, 136, 1070–1081

Table 1. Crystal Data for 3a

P, GPa	0[a]	1.8	4.4	6.0	9.8	11.1	13.0
phase	*α*-**3a**	*α*-**3a**	*β*-**3a**	*β*-**3a**	*γ*-**3a**	*γ*-**3a**	*γ*-**3a**
formula	$C_6HN_2OS_4$	$C_6HN_2OS_4$	$C_6HN_2OS_4$	$C_6HN_2OS_4$	$C_6HN_2OS_4$	$C_6HN_2OS_4$	$C_6HN_2OS_4$
M	245.33	245.33	245.33	245.33	245.33	245.33	245.33
a, Å	27.873(3)	26.436(2)	13.211(3)	12.880(2)	13.063(2)	13.001(2)	12.919(2)
b, Å	31.252(3)	29.579(3)	15.162(4)	14.888(4)	14.945(3)	14.909(3)	14.842(2)
c, Å	4.0004(5)	3.6728(2)	3.3733(6)	3.2737(5)	3.0230(3)	2.9950(3)	2.9619(3)
V, Å^3	3485.2(7)	2872.0(2)	675.7(2)	627.7(2)	590.2(1)	580.5(1)	567.9(1)
ρ_{calcd} (g cm^{-1})	1.870	2.270	2.412	2.596	2.761	2.807	2.870
space group	*Fdd*2	*Fdd*2	$Pbn2_1$	$Pbn2_1$	$Pbn2_1$	$Pbn2_1$	$Pbn2_1$
Z	16	16	4	4	4	4	4
temp (K)	296(2)	293(2)	293(2)	293(2)	293(2)	293(2)	293(2)
λ (Å)	0.6889	0.41337	0.41337	0.41337	0.41337	0.41337	0.41337
solution method	direct methods	powder data[b]	powder data[c]	powder data[c]	powder data[b]	powder data[b]	powder data[b]
R, R_w (on F^2)	0.0235, 0.0524	0.0046, 0.0061	0.0064, 0.0111	0.0049, 0.0085	0.0059, 0.0083	0.0062, 0.0087	0.0056, 0.0076

[a]See ref 28e. [b]Rietveld refinement. [c]Le Bail refinement.

therefore set out to explore the effect of physical pressure on the structure and transport properties of this material, to see if it could be metallized under relatively mild loadings, as in the case of **3b**.[28d] To our surprise, crystallographic measurements over the pressure range 0−13 GPa have revealed an unexpected structural response involving a stepwise conversion into two new phases, near 3 and 8 GPa. The architectural changes accompanying these phase transitions restore the coplanarity of the previously ruffled molecular ribbons, and the consequent solid-state electronic reorganization leads to a rapid increase in conductivity and decrease in activation energy, with eventual closure of the Mott−Hubbard gap and formation of a metallic state in the region of 4−5 GPa. The electronic structure of **3a** has been probed, at both the molecular and solid-state levels, by means of density functional theory (DFT) calculations; the results of which shed light on the reasons behind the enhanced charge transport properties of this class of radical conductor.

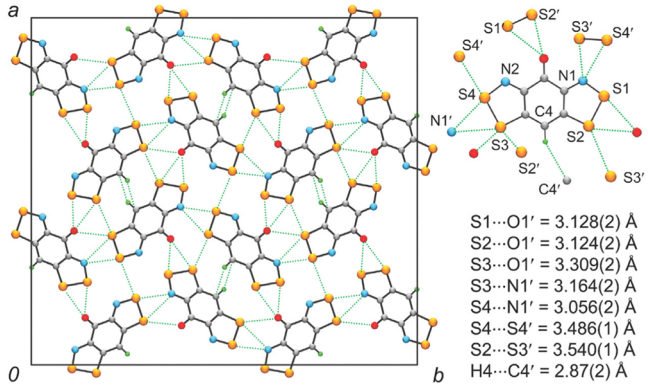

Figure 2. Unit cell drawing of the *α*-phase of **3a** at 0 GPa, showing intermolecular S···N′, S···O′, S···S′, and CH···C′ contacts (dashed lines).

RESULTS

High Pressure Crystallography. The effect of pressure on the crystal structure of **3a** has been examined by powder X-ray diffraction (XRD) over the range 0−13 GPa. Three phases have been identified, including the ambient pressure or *α*-phase, which was initially characterized by single crystal XRD methods.[28e] In the powder diffraction work, over 20 data sets were collected with increasing pressure, using synchrotron radiation and diamond anvil cell techniques. Subsequent indexing and space group elucidation revealed the conversion of the *α*-phase into a second or *β*-phase near 3−4 GPa and a third or *γ*-phase near 8 GPa. Structural solutions, determined using synthetic annealing methods, were based on the molecular geometry obtained from the single crystal structure determination at 0 GPa. During the initial Rietveld refinements, a rigid-body constraint was employed, but in the final Rietveld refinements of the *α*- and *γ*-phases and in the Le Bail refinements of the *β*-phase,[32] only the unit cell parameters were optimized. Crystal data from the final powder refinements are summarized in Table 1; intramolecular metrics, which are nominal for this class of radical, are available in the Supporting Information (SI).

Crystals of the *α*-phase of **3a** belong to the polar orthorhombic space group *Fdd*2 and consist of evenly spaced radical *π*-stacks running parallel to the *c*-axis. The unit cell drawing in Figure 2 (at 0 GPa) provides a projection (down the *π*-stacks) of the 16 symmetry related radicals ($Z = 16$) and illustrates the ribbon-like motifs (Figure 1) generated by the mutually perpendicular *d*-glide planes that traverse the cell in the *x* and *y* directions. Also shown is the network of short (within the standard van der Waals' separation)[33] intermolecular S···N′, S···O′, S···S′, and CH···C′ contacts that lace the structure together laterally. Of these the CH···C′ contacts, which bridge molecules up and down along the 2_1 axes, are of particular importance. These edge-to-face or tilted-T interactions[34] serve as cross connectors between the mutually orthogonal ribbons, as illustrated in Figure 3. In so doing, however, they cause a ruffling of the otherwise planar ribbons, to produce dihedral angles of ϕ_{bc} and ϕ_{ac} (Table 2), respectively, along the ribbons perpendicular to the *x* and *y* directions.

Initial pressurization of the *α*-phase leads to a decrease in the unit cell dimensions (Figure 4), the ease of compression of the *π*-stacks giving rise to a more pronounced contraction of the *c*-axis. At pressures above 3 GPa, the diffraction pattern changes substantially, heralding the formation of the *β*-phase. Attempts to index the data in the mixed phase region between 3 and 4 GPa were unsuccessful, but above 4 GPa the data could be fully analyzed in terms of a single *β*-phase. During initial indexing attempts, however, it became apparent that the *F*-centering found in the *α*-phase was not present in the *β*-phase. After consideration of all primitive orthorhombic (and monoclinic)

dx.doi.org/10.1021/ja411057x | J. Am. Chem. Soc. 2014, 136, 1070−1081

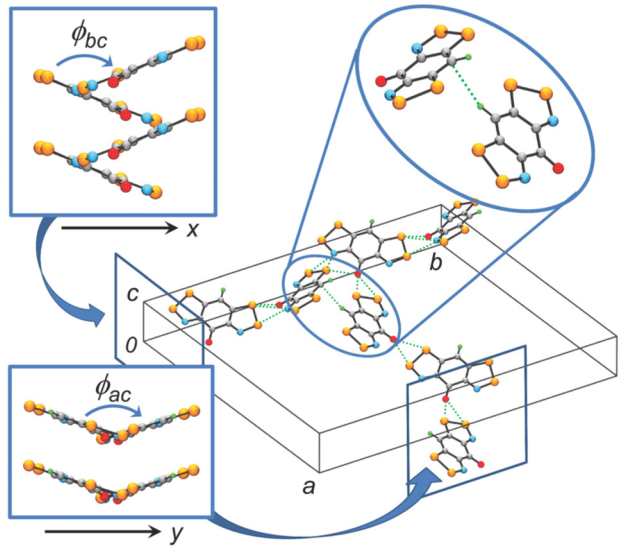

Figure 3. Ruffled ribbons of radicals, running perpendicular to the *x* and *y* directions, and linked by edge-to-face CH···C′ contacts. Extent of ruffling defined by dihedral angles ϕ_{bc} and ϕ_{ac}, with ϕ = 180° representing unruffled ribbons.

Table 2. Supramolecular Metrics for 3a

phase	*P* (GPa)	δ (Å)[a]	τ (°)[b]	ϕ_{bc} (°)[c]	ϕ_{ac} (°)[c]
α	0	3.47	29.8	135.7	142.4
α	1.84	3.23	28.5	137.7	143.6
β	4.4	2.84	32.8	177.5	114.5
β	6.0	2.80	31.1	179.9	117.8
γ	9.8	2.83	20.8	138.6	169.5
γ	11.1	2.80	21.0	139.1	170.6
γ	13.0	2.77	20.6	140.5	168.7

[a]δ is the separation of the mean molecular plane along the π-stacks. [b]τ defines the inclination of the π-stacks with respect to the *c*-axis. [c]The dihedral angles ϕ_{bc} and ϕ_{ac} are defined in Figure 3.

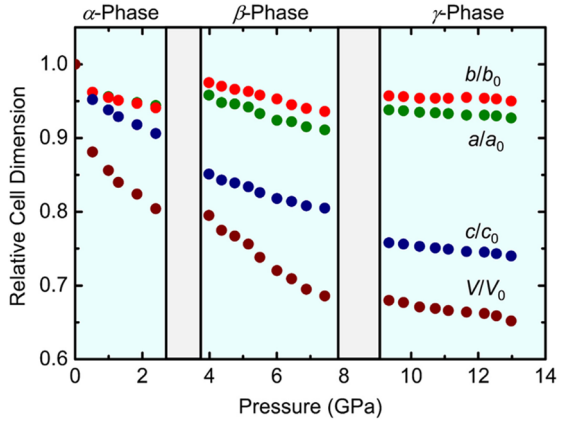

Figure 4. Relative dimensions of the unit cell parameters of **3a** as a function of pressure at room temperature. The *a*- and *b*-axes of the β- and γ-phases are scaled to allow comparison with those of the α-phase.

alternatives, only $Pbn2_1$ and $Pna2_1$ represented viable space groups for the β-phase. In both of these one of the *d*-glides of the α-phase evolves into an *n*-glide, while the other is transformed into an *a*- or *b*-glide, depending on the setting. The choice between the two was not easy to make, as most data sets could be indexed in either space group, and for some, preliminary structural solutions (in DASH) could also be obtained. However, only in the case of $Pbn2_1$ could *all* the β-phase data sets be solved (with preservation of the original setting established by the α-phase) and Le Bail refinements successfully achieved. With loss of *F*-centering the *a*- and *b*-axes are both halved in length, and *Z* collapses from 16 to 4. A representative unit cell drawing for the β-phase, obtained from the 6.0 GPa data set, is illustrated in Figure 5. Relative cell

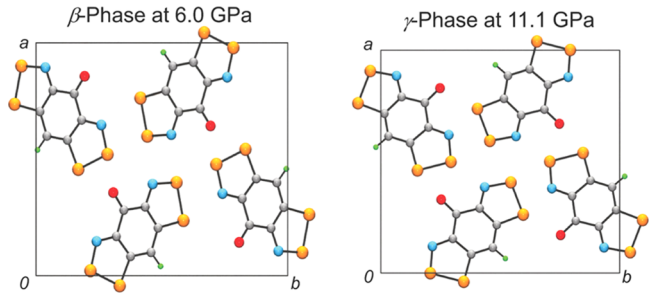

Figure 5. Unit cell of the β-**3a** at 6.0 GPa (left) and γ-**3a** at 11.1 GPa (right), viewed down the π-stacking *c*-axis.

dimensions of the β-phase (scaled to allow comparison with the α-phase) over the range 4−8 GPa are plotted in Figure 4, and details of two Le Bail refinements are listed in Table 1. Inspection of the results indicates that the α- to β-phase transition is associated with a pancake-like collapse of the unit cell, that is, the *c*-axis contracts, while the *a*- and *b*- axes elongate.

Further compression of the β-phase to 8 GPa gives rise to a uniform response along all three axes, with an overall compressibility similar to that found for the α-phase. Between 8 and 9 GPa a second phase transition takes place, but in this case there is no change in space group; like the β-phase, the emergent γ-phase is also $Pbn2_1$. As in the α- to β-phase transition the β- to γ-phase crossover is characterized (Figure 4) by a pancake-like collapse of the unit cell; the *a* and *b* dimensions increase, while *c* decreases. Once produced, however, the γ-phase is less compressible than either the α- or β-phase; all the cell dimensions remain relatively constant from 9 to 13 GPa (the limit of the measurements). Details of three representative Rietveld refinements are provided in Table 1, and the unit cell drawing shown in Figure 5 for the γ-phase at 11.1 GPa illustrates the similarity in packing in the *ab* plane to that found for the β-phase. The differences between the two phases are more apparent in the arrangement of the π-stacks, which is described below.

Having established the changes in cell dimensions of the three phases as a function of pressure, the next challenge was to characterize, at the molecular level, the structural differences between the three phases. In view of the fact that the structural solutions were based on rigid-body refinements, and also because of the complex network of intermolecular interactions which exist even at ambient pressure, we have not attempted to examine changes in intra- or intermolecular distances in detail. Rather, we have focused our analysis of the molecular packing within the three phases on the differences in the slippage of the π-stacks and their potential to interlock so as to afford regular (coplanar) molecular ribbons.

To this end we list in Table 2 a set of angles and distances which collectively provide a framework within which to compare changes in the supramolecular architecture of the

dx.doi.org/10.1021/ja411057x | J. Am. Chem. Soc. 2014, 136, 1070−1081

three phases. The most intuitive variables in this set are δ, the interplanar spacing of radicals along the π-stacks, and τ, the tilt or inclination angle of π-stacks to the c-axis. As expected, the value of δ decreases with increasing pressure and does so quite markedly with the α- to β-phase transition. The concomitant changes in τ are more subtle; there is a small increase with the first phase transition, then a larger decrease with the second, which heralds a more nearly superimposed alignment of the π-stacks as the effects of the concertina compression take hold. As illustrated in Figure 6, the packing of the β-phase (at 6.0 GPa)

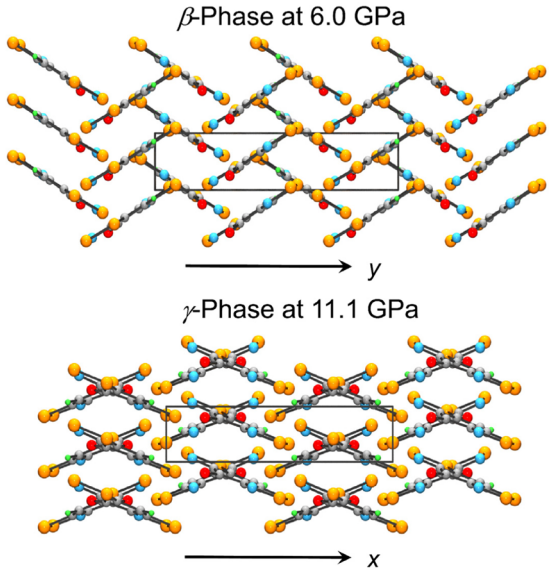

Figure 6. Cross-braced slipped π-stacks of β-**3a** (at 6.0 GPa), viewed perpendicular to the bc plane (above), and of γ-**3a** (at 11.1 GPa), viewed perpendicular to the ac plane (below).

consists of cross-braced π-stacks spanning layers perpendicular to the bc plane. The near-180° value of the dihedral angle ϕ_{bc} (Table 2) signifies a nearly coplanar arrangement of radicals along the ribbons within this array. At the same time, the degree of cross-bracing can be measured in terms of the other dihedral ϕ_{ac}, which becomes smaller (less obtuse) than in the α-phase. With the transition to the γ-phase, there is no change in space group, but the cross-braced π-stack architecture is switched, so that the nearly coplanar molecular ribbons now run along the n-glides within the ac plane, as illustrated in Figure 6. These changes are quantified by the reversal in the magnitude of the dihedral angles ϕ_{bc} and ϕ_{ac} (Table 2).

While we have no definitive explanation for the cause of the switching of the cross-braced π-stacks from being perpendicular to the bc plane in the β-phase to being perpendicular to the ac plane in the γ-phase, it is readily apparent (Figure 6) that in the β-phase neighboring layers are offset along y, whereas in the γ-phase there is no offset along x. Moreover, in the γ-phase neigboring radicals along each ribbon are slightly staggered, which may provide for more efficient packing at elevated pressure. Regardless, however, of the relative merits of the two possible arrangements, we note a striking similarity in the packing of both phases, but more particularly the β-phase, to the cross-bracing found in the ambient pressure structure of **3c**·MeCN (space group $Pna2_1$) reported previously.[28c]

High Pressure Infrared Conductivity. We reported earlier the results of ambient pressure, variable-temperature four-probe conductivity (σ) measurements on **3a**–**3e**.[28] Results

Table 3. Ambient Pressure Conductivity Data

radical	σ(300 K) (S cm^{-1})	E_{act} (eV)	ref
3a (R = H)	6.0×10^{-3}	0.16	28e
3b (R = F)	2.0×10^{-2}	0.10	28d
3c·MeCN (R = Cl)	3.0×10^{-3}	0.11	28c
3c (R = Cl)	4.0×10^{-3}	0.16	28c
3d (R = Me)	9.0×10^{-4}	0.13	28b
3e (R = Ph)	3.0×10^{-5}	0.20	28a

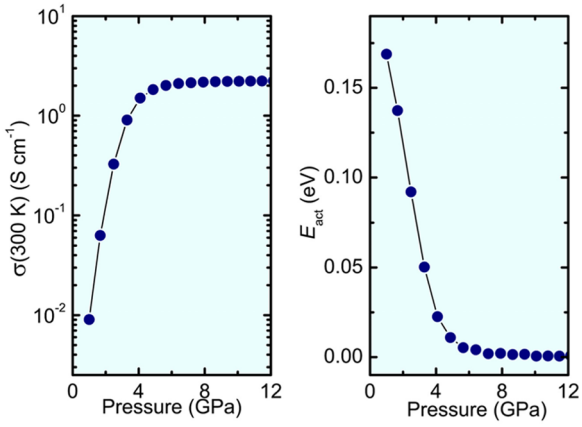

Figure 7. Pressure dependence of the conductivity σ(300 K) of **3a** and of its thermal activation energy E_{act} over the range T = 300–370 K.

for the entire set, expressed in terms of values of σ(300 K) and the Arrhenius activation energy E_{act} are summarized in Table 3. As may be seen therein, the conductivity of **3a** (R = H), σ(300 K) = 6×10^{-3} S cm^{-1}, lies near the top of the group, but its activation energy, E_{act} = 0.16 eV, is a little higher than that of **3b** or **3c**·MeCN. To explore the response of both of these parameters to applied pressure, we have carried out high pressure, variable-temperature conductivity measurements, using a 3000 ton press to scan pressure over the range 0–12 GPa. As may be seen in Figure 7, which illustrates the pressure dependence of both σ(300 K) and E_{act}, the latter measured between 300 and 370 K, compression causes an initial and rapid increase in σ(300 K), which reaches a plateau value near 2 S cm^{-1} at 6 GPa. There is little change thereafter out to 12 GPa. Across the same pressure range E_{act} drops sharply to near zero at 6 GPa, indicative of the formation of a weakly metallic state. In terms of potential correlations between the conductivity data and the phase changes for **3a** observed crystallographically, we note that the environment in the pressure cell used here is not purely hydrostatic. However, the fact that the α- to β-phase transition, accompanied by metallization, is recorded by conductivity gives confidence that the state of quasi-hydrostaticity would be sufficient to allow detection of a conductivity change at the β- to γ-phase transition, if there were one.

High Pressure Infrared Spectroscopy. To investigate the pressure-induced metallization of **3a** more closely, we have examined the pressure dependence of its solid-state infrared absorption and reflectance spectra, using diamond anvil cell techniques. At ambient pressures, discrete bands corresponding to molecular vibrational modes of the α-phase are discernible in the low-frequency regime of the absorbance spectrum (Figure 8). The strongest and most clearly visible of these corresponds to the CO vibration at 1600 cm^{-1}. With increasing pressure, between 2.7 and 4.1 GPa, the region of the α- to β-phase transition, the molecular modes are almost completely

dx.doi.org/10.1021/ja411057x | J. Am. Chem. Soc. 2014, 136, 1070–1081

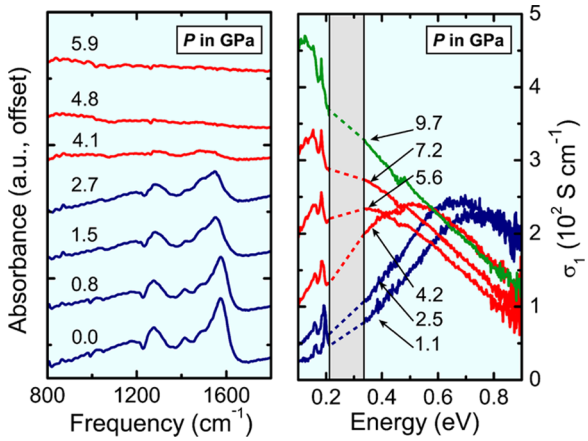

Figure 8. Pressure dependence of the ambient-temperature infrared absorption spectrum of **3a** (left). Pressure dependence of the ambient temperature optical conductivity σ_1 of **3a** (right). The three phases are color coded blue (α), red (β), and green (γ). The hatched zone on the right is obscured by diamond modes.

overwhelmed by the onset of a broad electronic absorption which shifts to lower energy with increasing pressure, as would be expected with the approach of a metallic state. Optical conductivity as a function of pressure (Figure 8) was obtained by Kramers–Kronig (K–K) analysis of normal incidence reflectivity measurements. For this purpose, strong phonon bands in the region from 1700 to 2700 cm^{-1} originating from the diamond cell were omitted by replacing this spectral region by a straight line interpolation. The resulting reflectivity data, after correction for the diamond refractive index, were then fit using a variational K–K constrained dielectric function, as implemented in the REFFIT code.[35]

At low pressures, in the α-phase, the optical conductivity shows a clear electronic excitation gap, with spectral density falling away at low frequencies, characteristic of insulating behavior. As expected in Mott insulators,[36] a broad peak in σ_1 is observed, centered at the energy scale for short-range charge fluctuations (in this case 0.7–0.8 eV), and with a total width that reflects the overall bandwidth. Upon compression to the β-phase, there is a large transfer of spectral weight from this high-frequency Hubbard feature to lower energies, suggesting rapid closure of the Mott gap, and the onset of a correlated metallic state. In the present study, the measured spectral window does not extend to sufficiently low frequencies to resolve properly any Drude-like features associated with coherent metallic carriers, which may become apparent below ~200 cm^{-1} (25 meV).[37] Commonly, such a Drude-like peak is found to coexist with higher energy Hubbard-like features, although at ambient temperatures, thermal fluctuations may significantly smear out this peak or even destroy the coherent excitations entirely.[38] While not directly observed in the optical conductivity, the build-up of low-energy charge excitations, for pressures exceeding 4.2 GPa, is indicated by (i) the significant shift of spectral weight (Figure 8), (ii) a plateau in the dc conductivity, and (iii) disappearance of the thermal activation energy (Figure 7). We therefore characterize the β-phase as a correlated metal with no charge gap but with residual incoherent excitations at high frequency due to charge correlation. Upon further compression to the γ-phase, such high-energy features are significantly suppressed but without enhancement of the dc conductivity, which remains below the minimum metallic conductivity expected for normal Fermi liquids.[39] This suggests significant correlation even in the γ-phase; the investigation of which provides an interesting focus for future work.

Molecular Electronic Structure Calculations. To compare the properties of the two families of radicals based on **1** and **3**, we have carried out a series of DFT calculations at the (U)B3LYP/6-311G(d,p) level on the two prototypal derivatives **1a** and **3a**. The frontier Kohn–Sham molecular orbitals for both species, the HOMO, SOMO, and LUMO, may be envisaged as originating from a coupling of the SOMOs of two 7π-electron dithiazolyl (DTA) radicals through the p_π orbital of the basal carbon (which provides one π-electron). In C_{2v} symmetry there are two DTA SOMO combinations, of a_2 and b_1 symmetry, but only the latter can mix with the carbon p_z orbital to afford in-phase (bonding) and out-of-phase (antibonding) b_1 combinations. Respectively, these two orbitals drop below and rise above the unperturbed a_2 combination, which becomes the SOMO of the hypothetical acyclic precursor (Figure 9). The impact on these frontier orbitals of

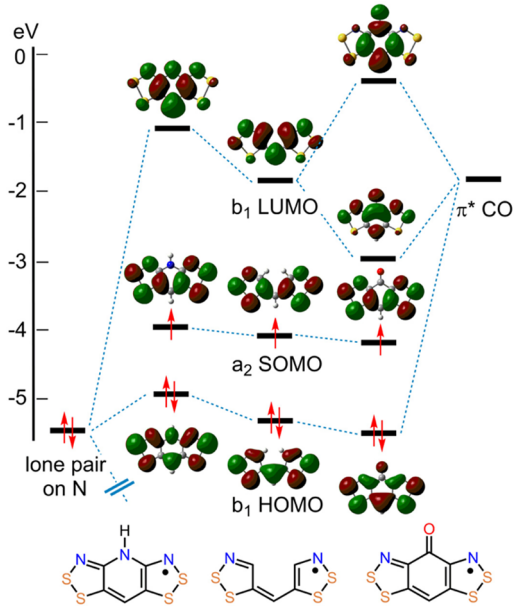

Figure 9. Correlation diagram tracking the (U)B3LYP/6-311G(d,p) π-frontier orbitals of **1a** (left) and **3a** (right), starting from a common acyclic radical precursor (center).

the inclusion of a NH fragment, to produce **1a**, and of a CO fragment, to afford **3a**, has been tracked by DFT calculations at the (U)B3LYP/6-311G(d,p) level.

The ground-state electronic structures of the two radicals are remarkably similar. By symmetry, incorporation of either a nitrogen lone pair or a carbonyl fragment into the frontier π-orbital manifold of the radical precursor does not, to first order, affect the energy or composition of the emerging a_2 SOMO. As a result the two radicals possess very similar spin distributions. Consistently the EPR spectra of all reported radicals **1**[19,22] and **3**[28] reveal comparable hyperfine coupling constants a_N that are approximately one-half of those found in monofunctional 1,2,3-dithiazolyls, as would be expected given that the spin density is "shared" between two DTA rings.[40] Moreover, given that the SOMO is nodal at the basal carbon and at the site of NH/CO interchange, there is very little variation in a_N values as a function of basal R-group. That being said, with the inclusion of charge repulsion effects there are some subtle but understandable changes in orbital energies (Figure 9). Thus, the DFT

dx.doi.org/10.1021/ja411057x | J. Am. Chem. Soc. 2014, 136, 1070–1081

SOMO of **1a** lies slightly higher than that of **3a**, an observation consistent with the differences in their oxidation potentials.[28]

The important differences between radicals **1** and **3** are more evident in their excited-state properties and related ion chemistry, which arise from variations in the energy of the two frontier orbitals of b_1 symmetry. Incorporation of an NH fragment into the carbon-bridged bisdithiazolyl precursor, to generate **1a**, leads to relatively strong mixing of the high-lying nitrogen lone pair with the HOMO and LUMO of the precursor, forming antibonding combinations with each and causing both to rise in energy (Figure 9, left).[41] By contrast, with the insertion of a carbonyl group to generate **3a**, the empty π^*(CO) orbital so introduced mixes strongly with the LUMO of the precursor to afford a new, much lower lying LUMO for **3a**. In reality both the filled π(CO) and empty π^*(CO) orbitals are capable of mixing with b_1 orbitals of the precursor, but the former is energetically much lower lying, and its effect on the frontier orbitals is relatively minor. Similar, albeit weaker mixing of the π^*(CO) acceptor level with the HOMO of the precursor also causes the latter to drop in energy, and the SOMO−HOMO gap to widen. The consequences of the larger HOMO−SOMO splitting in **3a** relative to **1a** are readily apparent in the optical spectra of the corresponding cations, in which the radical SOMO is no longer occupied. Thus the absorption maximum for the HOMO−LUMO excitation in the cation $[\mathbf{1a}]^+$ (λ_{max} = 650 nm)[22a] is significantly red-shifted relative to that of $[\mathbf{3a}]^+$ (λ_{max} = 554 nm).[28e]

With reference to the ion energetics of **3a**, the consequences of its low-lying π-LUMO are more profound, as the small SOMO−LUMO gap suggests that reduction to the anion $[\mathbf{3a}]^-$ may give rise to an open-shell state, a possibility in keeping with the theoretical predictions for related antiaromatic biscyanine dyes.[42] To explore this possibility we used DFT methods to examine the total energy of the anion in the closed-shell singlet state (CSS) and the triplet state (TS). The energy of the open-shell singlet state (OSS) could not be calculated directly but was assessed indirectly using the broken symmetry approach[43] to calculate the energy of the broken symmetry singlet state (BSS). Plots of the spin distributions for the BSS and TS states are illustrated in Figure 10.

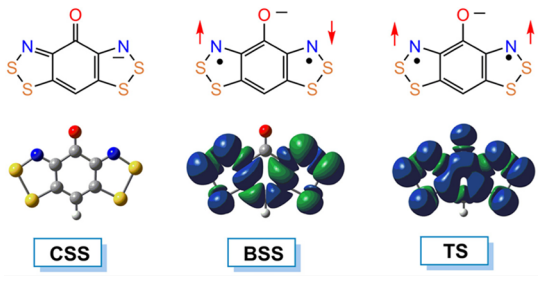

Figure 10. Valence-bond representations and (U)B3LYP/6-311G-(d,p) spin distributions (gas phase) for the CSS, BSS, and TS states of $[\mathbf{3a}]^-$. The a_2 and b_1 orbitals of **3a** are illustrated in Figure 9.

Numerical results are summarized in Table 4, which provides the relative energies of all four states with and without the (screening) effects of solvation; the latter were simulated using the polarized continuum model (PCM), with acetonitrile as solvent (as in the electrochemical work).[28] From an energetic standpoint all the open-shell states are predicted to be more stable than the CSS, with the triplet being the ground state.

Table 4. Relative State Energies[a] for $[\mathbf{3a}]^-$

	E^{TS} ($<S^2>$)	E^{BSS} ($<S^2>$)	E^{OSS}[b]	E^{CSS}
gas phase	0 (2.024)	0.70 (0.830)	1.17	4.79
PCM (MeCN)[c]	0 (2.027)	2.70 (0.956)	5.05	9.50

[a](U)B3LYP/6-311G(d,p) energies, in kcal mol^{-1}, of the CSS, BSS and OSS states, relative to the TS state. For the TS and BSS states $<S^2>$ expectation values are given in parentheses. [b]$E^{OSS} = E^{TS} - 2\,[E^{TS} - E^{BSS}]/[<S^2>_{TS} - <S^2>_{BSS}]$ (see ref 43). [c]PCM with MeCN as solvent.

Morever, the relative stability of the TS is increased by solvent polarity (as in MeCN), an effect readily appreciated in terms of its large molecular dipole moment (μ = 5.80 D, gas phase), which is substantially larger than that (μ = 3.25 D, gas phase) found for the CSS anion. That the open-shell states lie energetically below the CSS follows directly from the presence of the low-lying b_1 orbital on the radical, a feature not present in the corresponding anion $[\mathbf{1a}]^-$. Additional stabilization of the triplet arises from strong Hund's rule coupling between the a_2 and b_1 orbitals (a Fermi hole),[44] a situation not found in disjoint biradicals, which typically possess OSS ground states.[45]

Using the state energies of the anion $[\mathbf{3a}]^-$ provided in Table 4, we have calculated the associated electron affinity (EA) of the radical in the gas phase and MeCN solution (Table 5).

Table 5. Calculated Ion Energetics (eV)[a] and Electrochemical Potentials (V)[b] for 1a and 3a

	1a		3a	
	gas phase	PCM (MeCN)[c]	gas phase	PCM (MeCN)[c]
IP	6.16	4.41	6.51	4.61
EA^{CSS}	1.58	3.24	1.83	3.38
EA^{OSS}	–	–	1.99	3.57
EA^{TS}	–	–	2.04	3.79
$\Delta H_{disp}{}^{CSS}$	4.59	1.17	4.68	1.23
$\Delta H_{disp}{}^{OSS}$	–	–	4.52	1.04
$\Delta H_{disp}{}^{TS}$	–	–	4.47	0.82
$E_{1/2}$ (0/+1)	−0.130 (−0.170)[d]		0.061 (0.035)[d]	
$E_{1/2}$ (−1/0)	−0.946[e]		−0.525[e]	
E_{cell}	0.78[f]		0.56[f]	

[a](U)B3LYP/6-311G(d,p) IP, EA, and disproportionation enthalpies (ΔH_{disp} = IP − EA), all in eV; superscripts CSS, OSS and TS designate the appropriate anionic state. [b]Electrochemical potentials in V vs SCE (in MeCN solvent) for **1a** and **3a** taken from refs 22a and 28e. [c]PCM with MeCN as solvent. [d]Cathodic peak potential E_{pc} in parentheses. [e]Irreversible reduction, E_{pc} value cited. [f]E_{cell} estimated as $|E_{pc}(0/+1) - E_{pc}(-1/0)|$.

When taken with the calculated ionization potential (IP) for the radical, these EA values afford estimates of the disproportionation energy ΔH_{disp} as a function of the anionic state (CSS, OSS, and TS). These values then provide an estimate of the energy barrier to charge transport which, in a single orbital model, would be given by *U*. In the case of **1a** the analysis is restricted to the use of the closed-shell anion $[\mathbf{1a}]^-$, as there are no low-lying virtual π-orbitals in **1a** (Figure 9) available that can give rise to open-shell anions of π-symmetry.[41] However in the case of **3a** there are low-lying OSS and triplet anions $[\mathbf{3a}]^-$, the latter arising from strong Hund's rule coupling between the SOMO and LUMO of the radical, that lead to successive increases in EA and, in turn, reductions in the value of ΔH_{disp} (Table 5). While the overall difference between the two radicals is only marginal in the gas phase, the inclusion of solvation (screening effects) via the PCM model amplifies the separation

dx.doi.org/10.1021/ja411057x | J. Am. Chem. Soc. 2014, 136, 1070−1081

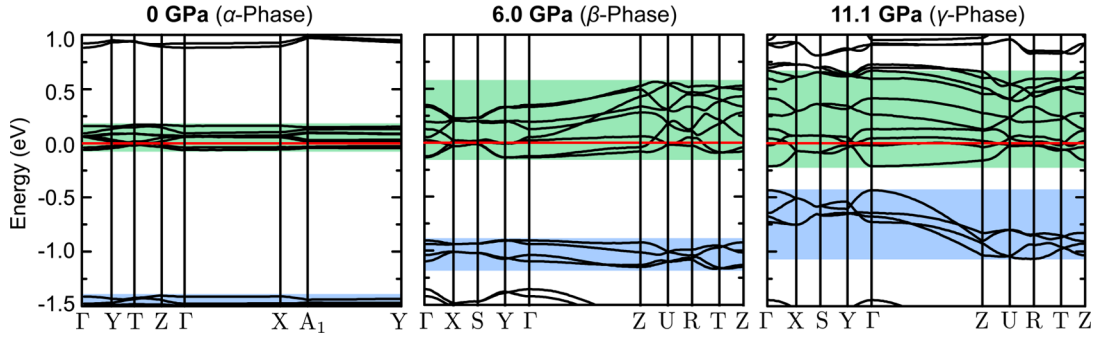

Figure 11. Crystal orbital dispersion of **3a** at 0, 6.0, and 11.1 GPa. Energy bands arising from the HOMO, and the overlapping SOMO and LUMO crystal orbitals, are highlighted. The Fermi level is shown as a red line at 0 eV.

considerably, and reproduces, at least qualitatively, the experimental differences in $E_{1/2}$ and E_{cell} values. Overall, we conclude that oxobenzene-bridged radicals are softer by virtue of their unusually high electron affinity, which can in turn be related to the presence of a low-lying π-LUMO. The effect of these energetic changes on the magnitude of U and charge transport is discussed below.

Band Structure Calculations. To probe the changes in the solid-state electronic structure of **3a** as a function of pressure we have carried out single point DFT band structure calculations with the Quantum Espresso package, using atomic coordinates taken from the crystal structures determined at 0, 6.0, and 11.1 GPa; these three pressures provide representative snapshots of the α-, β- and γ-phases. The results are shown in Figure 11 in the form of crystal orbital band dispersion diagrams over a range of reciprocal space directions in the first Brillouin zone. In all cases the calculations were performed assuming a nonmagnetic state so as to be able to make a direct comparison of the degree of band spreading at the different pressures. As expected, the pattern of bands near the Fermi surface follows directly from frontier orbital ordering observed in the single molecule calculations, with three groups of four bands (Z = 4 in the primitive cell), arising from HOMO, SOMO, and LUMO. There is a relatively large gap between the HOMO and SOMO bands, while in the reduced symmetry of the crystal the SOMO and LUMO bands are almost coincident.[46]

At 0 GPa the bandwidth of all three bands is small. Indeed, the heavily overlapped SOMO and LUMO bands give rise to a total bandwidth of < 0.3 eV, and on this basis it is not surprising that the α-phase structure is a Mott insulator. However, with pressurization to 6.0 GPa and formation of the β-phase, there is considerable spreading of all three bands. Moreover, with the relaxation of the orthogonality constraints found at the molecular level, the SOMO and LUMO bands are strongly mixed, to afford a combined bandwidth near 0.7 eV, that is, on the same order as the Coulomb barrier estimated from the IR measurements presented above. Further compression to 11.1 GPa, and evolution to the γ-phase, lifts the HOMO band, and higher lying virtual orbitals drop, so as to produce a more congested array near the Fermi level, and a composite partially filled band with bandwidth near 1.0 eV.

DISCUSSION

The predisposition of oxobenzene-bridged bisdithiazolyls **3** to crystallize as coplanar ribbon-like arrays linked by intramolecular S···N′ and S···O′ contacts affords an appealing structural handle for the design of new solid-state architectures for neutral radical materials. The differences in the charge-transport properties within the series **3a**−**3e** can be ascribed, in part, to variations in the way these molecular ribbons are packed, as the degree of offset between consecutive layers produces materials whose electronic structures range from strongly 1D (for **3e**) to perfectly 2D (in **3b**). In the case **3a** (R = H) the ribbons are ruffled (Figure 3) at ambient pressure by edge-to-face CH···C′ contacts, as a result of which offset layering of the ribbons is not possible, and a relatively 1D structure with low bandwidth prevails. Consistently, its ambient pressure performance, measured in terms of E_{act} values, does not rise to that found for **3b** or **3c** (Table 3). However, with the pressure-induced structural changes occasioned by the α- to β-phase transition, which produce cross-braced, coplanar ribbons (Figure 6) akin to those seen in **3c**·MeCN,[28c] there is a significant increase in bandwidth and consequent decrease in E_{act}. The second phase transition, to the γ-phase, is associated with a crossover of the ribbon-like arrays from the *b*-glides to the *n*-glides of the $Pbn2_1$ space group. With further compression of the γ-phase, neighboring radicals along the molecular ribbons slide over one another, like tiles on a roof, a process which gives rise to increased bandwidth relative to the β-phase. Thus, while the α-phase of **3a** gets off to a bad start, formation of the β- and γ-phases improves its transport properties dramatically.

The larger question, however, is related not to the differences within the set of known oxobenzene-bridged radicals **3** but rather to their common features, notably their charge transport properties, gauged in terms of their high σ(300 K) and low E_{act} values,[28] which set them apart from other thiazyl radical conductors, notably the isolectronic N-alkyl pyridine-bridged materials **1**.[19,22] While packing differences (layered ribbons versus herringbone arrays) may give rise to improvements in bandwidth, the electrochemical properties of all oxobenzene-bridged radicals, notably their consistently lower cell potentials E_{cell},[28] suggest they are electronically softer than the structurally related N-alkyl pyridine-bridged variants. This result arises from the preference for open-shell anionic states (Table 4) occasioned by the occupation of the low-lying LUMO. The consequent electronic softening, manifest in an increase in EA, lowers the calculated ΔH_{disp} values of **3a** on the order of 0.22 eV (in solution) compared to those of **1a**. The consequent reduction in the charge gap leads to an enhancement in conductivity, and in the case of **3a** (and **3b**) is sufficient to permit formation of a metallic state under relatively mild pressure.

Pressure-induced Mott insulator to metal transitions have been observed in other organic materials, notably in the κ-phase

dx.doi.org/10.1021/ja411057x | J. Am. Chem. Soc. 2014, 136, 1070−1081

salts of BEDT-TTF or ET, which possess the general formula $[ET]_2[X]$, where X is, for example, $Cu[N(CN)_2]Cl$.[47] In these materials, the involvement of closely spaced frontier orbitals in improving electronic softness is well recognized. The electronic structure of the dimer radical cation $[ET]_2^{\bullet+}$ building blocks (Figure 12) can be described in terms of a three-electron two-

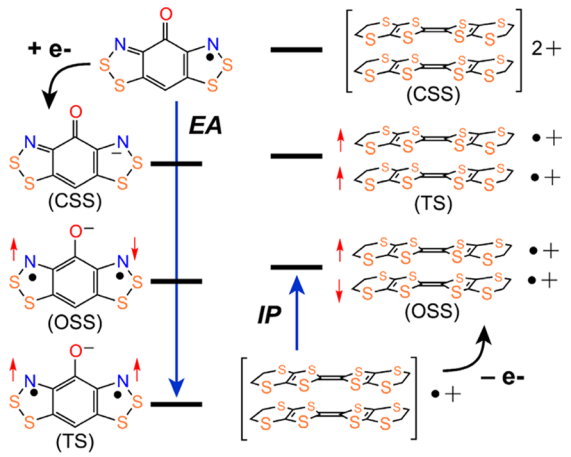

Figure 12. Energetic ordering of closed- and open-shell ionic states arising from electron addition to **3a** and electron removal from $[ET]_2^{\bullet+}$. For **3a**, the TS is the ground state of the resulting anion, while for $[ET]_2^{\bullet+}$, the resulting dication admits an OSS ground state. In both cases, the CSS lies higher in energy than both open-shell states. The energetically favorable open-shell states result in a reduction in ΔH_{disp} = IP − EA, by either increasing EA for **3a**, or reducing IP for $[ET]_2^{\bullet+}$.

orbital $(\pi)^2(\pi^*)^1$ configuration, where the π and π^* orbitals are weakly separated bonding and antibonding combinations of the HOMO of a single, neutral ET molecule. Due to the small π–π^* splitting in the dimer radical cation, removal of an electron (or addition of a hole) results in a charge separated, OSS state with configuration $[(\pi)^2(\pi^*)^0 - (\pi)^0(\pi^*)^2]$ rather than a closed-shell dication $(\pi)^2(\pi^*)^0$. This ability of the dimer to accommodate multiple charges on separate monomers decreases the ionization potential of the dimer cation relative to the monomer, ultimately providing a low $\Delta H_{disp}^{OSS} \sim 0.4$ eV. This low value for the Coulomb barrier is directly responsible for allowing metallic states which can be accessed in such salts. Despite the open-shell, multi-orbital description of the dication, ET salts are treated theoretically with a single-band Hubbard model, which requires only that the empty site (dication) be a singlet.

The above picture is in contrast to the situation found in **3a**, where a single molecular site, doubly occupied by electrons, possesses a triplet ground state. As this state is not found in the single-band model, explicit consideration of multiple orbitals and strong Hund's rule coupling is required. Calculations suggest the relevant orbitals for consideration are the SOMO and low-lying LUMO which, in the solid state, are significantly mixed at the DFT level due to the reduction of symmetry, providing a nearly degenerate pair of bands. More generally, this mixing should be a strong function of pressure[48] and is likely overestimated by insufficiently correlated methods such as DFT. In this sense, and apart from the observed structural phases transitions in **3a**, the interplay between orbital, charge, and magnetic degrees of freedom in **3** is potentially very rich. As an example of a magnetic effect, the combination of a low-lying LUMO and strong Hund's rule coupling is known to generate ferromagnetic interactions through excited-state mixing.[49] This mechanism is almost certainly responsible for the ferromagnetic Weiss constant Θ = +15.6 K observed at ambient pressure for **3a**.[28e] In regard to charge transport properties, Hund's rule coupling has been suggested to play a "Janus-faced" role.[50] Thus, while Hund's coupling clearly reduces the Coulomb barrier for parallel spins (ΔH_{disp}^{TS}), promoting the metallic state, it has also been associated with strongly reduced charge carrier stability and "bad metal" states with a vanishing E_{act}, but conductivity below the minimum value for a Fermi liquid. In the so-called Janus-faced region, where such states are prevalent, the electronic bandwidth W exceeds the Coulomb term for parallel spins, that is $U_{eff} \sim \Delta H_{disp}^{TS}$, but not for antiparallel spins, that is $U_{eff} \sim \Delta H_{disp}^{OSS}$. As such properties appear to characterize the high-pressure phases of **3a**, we believe further exploration of the ramifications of multiorbital Hund's physics in the neutral radical family **3** and related compounds represents an interesting avenue for future investigation.

SUMMARY AND CONCLUSION

As a result of the demanding energetic constraints of the classical one-electron, one-orbital neutral radical conductor model, the struggle to enhance the generally weak intermolecular interactions found in crystalline molecular radicals, to the point that the electronic bandwidth W offsets the onsite Coulomb potential U, has proven an *almost* insurmountable task. The well-known strategy of moving away from the half-filled band position, as in spiro-biphenalenyls[9a] or by chemical doping,[18] provides a remarkably effective mechanism for lowering U. It now appears that in resonance stabilized oxobenzene-bridged bisdithiazolyl radicals **3** a similar end is achieved, but by a different means. The low-lying π-acceptor level introduced by the replacement of the NR_1 group in **1** by a CO moiety in **3** has a significant impact on the ion energetics of the resulting radical, which becomes electronically softer by virtue of an enhanced electron affinity arising from the presence of low lying open-shell anionic states. The consequent reduction in U, coupled with strong SOMO–LUMO band mixing in the solid state, leads to enhanced conductivity of all radicals **3** relative to their analogues **1**.

While the prototypal radical **3a** represents, in principle, an excellent low-U building block, its ruffled-ribbon crystal structure is not ideal for generating good bandwidth. However, as described here, the crystal packing is very receptive to pressure-induced structural adjustments, as witnessed by the occurrence of not one but two phase transitions below 10 GPa. The onset of metallization is hard to pinpoint exactly, as different techniques suggest different values, but it appears to be closely associated with the α- to β-phase change, that is at $P \sim 4$ GPa. DFT band structure calculations show a significant increase in bandwidth in the β-phase, which is further enhanced as a result of the second transition to the γ-phase. Overall we believe that the low-lying LUMO effect described here provides important insight into the design of radical-based conductors. It remains to be seen whether continued exploration of the known derivatives **3a**–**3e** under pressure will reveal new electronic features, such as superconductivity. It may also be possible to design radicals in which the low-lying LUMO effect is more pronounced, so as to afford single component $f = {}^1/_2$ materials that are metallic, perhaps even superconducting, without the need for applied pressure.

dx.doi.org/10.1021/ja411057x | J. Am. Chem. Soc. 2014, 136, 1070–1081

EXPERIMENTAL SECTION

Sample Preparation. Microcrystalline samples of **3a** suitable for high-pressure measurements were generated by reduction of the salt [**3a**][ONf] (ONf = nonafluoromethanesulfonate) with octamethylferrocene in degassed acetonitrile. Details of the preparation and reduction of [**3a**][ONf] are described elsewhere.[28e]

Crystallography. High-pressure diffraction experiments on **3a** were performed at BLX10U, SPring-8, using synchrotron radiation (λ = 0.41337 Å) and a powdered sample mounted in a diamond anvil cell (DAC), with helium as the pressure transmitting medium. (At room temperature, helium stays in a liquid state up to 14 GPa, hence providing hydrostatic pressure conditions). A total of 23 data sets were collected over the range 2θ = 3−20° at room temperature and as a function of *increasing* pressure from 0 to 13.0 GPa. Space group determinations, indexing, and refinement of cell parameters were performed using DASH 3.1.[51] Structural solutions were also carried out in DASH, starting from a model based on the atomic coordinates taken from the ambient pressure structure determined by single crystal methods.[28e] During the Rietveld[52] refinement in DASH a rigid-body constraint was maintained.[53] The cell settings and atomic coordinates from the DASH solutions were then taken into GSAS[54] for a final Le Bail[55] and/or Rietveld refinement. The data from 2θ = 3−13° were refined with fixed atomic positions and isotropic thermal parameters with an assigned value of 0.025.

Conductivity Measurements. High-pressure conductivity experiments on **3a** were performed in a 3000 ton multi-anvil press using a Cr_2O_3-doped MgO octahedron as the pressure transmitting medium.[56] The pressure was generated by four electric oil pumps, transmitted through a split-cylinder module to six steel anvils, then to eight tungsten carbide (WC) cubes with 32 mm edge length, and finally through the eight truncated corners of these cubes to the octahedral pressure medium. The force−pressure relationship for the 18/11 (octahedral edge length (mm)/truncated edge length (mm)) cell configuration adopted in this experiment was determined from prior calibrations of the applied hydraulic load against pressures of structure transformations in standards at room temperature (Bi I ↔ II at 2.55 GPa, Bi III ↔ V at 7.7 GPa, and Sn I ↔ II at 9.4 GPa). The pressure cell was modified to include a cylindrical heater folded from a rhenium (Re) foil of 0.05 mm thickness and a $W_5Re_{95}/W_{26}Re_{74}$ thermocouple with its junction placed in contact with the outside wall of the Re heater. Powder samples were densely packed in a boron nitride (σ_{BN} = 10^{-11} S cm^{-1}) cup with Pt disk electrodes in direct contact with the samples at both ends. Four wire ac (Solartron 1260 Impedance Analyzer) resistance measurements were made at a frequency of 1 kHz. A series of resistance measurements was performed at pressures up to 12.2 GPa and temperatures up to 370 K. In each series, the pressure was first increased to the target value, and then resistance measurements were made at fixed temperature intervals of 10 °C on heating/cooling at constant pressure. The contiguous cylinder-shaped sample was extracted from the recovered pressure cell, and the sample geometry was measured to convert resistance to conductivity.

Infrared Measurements. High-pressure infrared absorption measurements on **3a** were performed at the Canadian Light Source using a Sintek mini DAC, equipped with type IIa diamond anvils and 300 μm culets. The spectra were recorded on a Hyperion 3000 IR microscope with a liquid nitrogen cooled MCT detector. A stainless-steel gasket with an initial thickness of 250 μm was preindented in the mini DAC to a final thickness of ∼140 μm, and a 100 μm hole was drilled at the center of the indentation that served as a sample chamber. A small amount of finely grounded KBr was then loaded in the sample chamber and was made transparent by gently tightening the DAC along with a ruby sphere (pressure marker). A small amount of **3a** was then transferred on to the transparent KBr for high-pressure measurements. We used ∼100 and ∼50 μm samples, respectively, for the globar and synchrotron measurements. Spectral data collection employed a resolution of 4 cm^{-1} and 512 scans. Pressure measurements were calibrated using the R_1 ruby line fluorescence, and absorption of the anvils and KBr was used as the background spectrum.

A symmetric DAC including a pair of synthetic type IIa diamond anvils with 400 μm culet was employed for high-pressure infrared reflectivity measurements recorded at the National Synchrotron Light Source (NSLS) at Brookhaven National Laboratory. A T-301 stainless-steel gasket was preindented to ∼40 μm thick, and a 200 μm hole was drilled in the center of the indentation to serve as the sample chamber. The **3a** sample powder was squeezed into a pellet using the DAC. The extra sample was removed from the anvil culet that the sample pellet attached to and left the rest of the sample in the center with ∼200 μm in diameter to match the gasket hole. The sample pellet was then loaded into the sample chamber together with precompressed KBr as a pressure transmitting medium and a ruby ball as a pressure marker. Reflectivity experiments were performed at the U2A beamline side-station of the NSLS. Infrared spectra were collected using a Bruker Vertex 80v FTIR spectrometer and a Hyperion 2000 IR microscope attached with a liquid nitrogen cooled MCT detector. To eliminate any contaminated signal from the gasket, a confocal configuration was employed to match the infrared beam spot and selected sample area of 20 × 20 μm. A conventional globar source was used to minimize any intensity fluctuation during the measurements. In addition, the diamond−air surface was used as the reference at each pressure point. A KBr beamsplitter was used to cover the mid-IR region with a spectral resolution of 4 cm^{-1}.

Optical conductivity was obtained by Kramers−Kronig (K−K) analysis of data obtained from normal incidence reflectivity measurements, then fit using a variational K−K constrained dielectric function, as implemented in the REFFIT code.[35] Since the K−K integrals relating real and imaginary parts of the dielectric function are taken over all frequencies, obtaining the complex dielectric function from reflectivity analysis requires, in principle, data over a wide frequency range. However, since the kernel of such integral transformations is strongly peaked at the frequency of interest, the form of the optical conductivity can be obtained for frequencies where reflectivity data is available, provided a sensible approximate form for the dielectric function is chosen outside this region. In the present case, various choices for the approximate form lead to ambiguity in the absolute magnitude of the optical conductivity, but preserve the main spectral features.

Molecular Electronic Structure Calculations. All DFT calculations were performed with the Gaussian 09W suite of programs,[57] using the (U)B3LYP hybrid functional and polarized, split-valence basis sets with triple-ζ (6-311G(d,p)) functions. Full geometry optimization was invoked for the calculation of the total self-consistent field (SCF) energies of radical, cation, and anion states of **1a** and **3a**, from which gas-phase IP and EA values were derived. In addition, for **3a** the triplet and BSS anionic states were also examined (using tight convergence criteria). The PCM was invoked to assess the effects of solvation on all these states.

Band Electronic Structure Calculations. Band structure calculations were carried out with the QUANTUM ESPRESSO[58] package using the Perdew−Burke−Ernzerhof functional and ultrasoft pseudopotentials with a plane-wave cutoff of 25 Ry and a 250 Ry integration mesh. Geometrical coordinates were taken from the single crystal or GSAS refined structures at 0 GPa (α-phase), 6.0 GPa (β-phase), and 11.1 GPa (γ-phase), and calculations were performed on the primitive cell. For the α- (β-, γ-) phases, SCF calculations employed a 4 × 4 × 4 (4 × 4 × 8) Monkhorst−Pack k-point mesh.

ASSOCIATED CONTENT

Supporting Information

Complete refs 57 and 58. Details of high-pressure crystallographic data collection and structure refinement for **3a**, and Gaussian 09 archive files. This information is available free of charge via the Internet at http://pubs.acs.org.

AUTHOR INFORMATION

Corresponding Author

oakley@uwaterloo.ca

Notes

The authors declare no competing financial interest.

■ ACKNOWLEDGMENTS

We thank the Natural Sciences and Engineering Research Council of Canada (NSERCC) for financial support. We also thank the NSERCC for a Vanier Graduate Scholarship to K.L. and a Graduate Scholarship to S.M.W., the Government of Canada for a Tier I Canada Research Chair to J.S.T., the Japan Synchrotron Radiation Research Institute (JASRI) for beam time, and the Canada Foundation for Innovation for funding a 300 ton multi-anvil press. Research performed at the Canadian Light Source was funded by the NSERCC, the Canada Foundation for Innovation, the National Research Council Canada, the Canadian Institutes of Health Research, the Government of Saskatchewan, Western Economic Diversification Canada, and the University of Saskatchewan. The use of the U2A beamline at the NSLS is supported by NSF (EAR 06-49658, COMPRES) and DOE/NNSA (DE-FC03-03N00144, CDAC). NSLS is supported by the DOE/BES (DE-AC02-98CH10886). The high-pressure XRD experiments at SPring-8 were performed under proposal no. 2012A1225 (by J.S.T.).

■ REFERENCES

(1) McCoy, N. H.; Moore, W. C. *J. Am. Chem. Soc.* **1911**, *33*, 273.

(2) (a) Bendikov, M.; Wudl, F.; Perepichka, D. F. *Chem. Rev.* **2004**, *104*, 4891. (b) Jérome, D. *Chem. Rev.* **2004**, *104*, 5565. (c) Geiser, U.; Schlueter, J. A. *Chem. Rev.* **2004**, *104*, 5203. (d) Yamada, J.; Akutsu, H.; Nishikawa, H.; Kikuchi, K. *Chem. Rev.* **2004**, *104*, 5057. (e) Saito, G.; Yoshida, Y. *Bull. Chem. Soc. Jpn.* **2007**, *80*, 1. (f) Saito, G.; Yoshida, Y. *Top. Curr. Chem.* **2012**, *312*, 67.

(3) (a) Mott, N. F. *Proc. Phys. Soc., London, Sect. A* **1949**, *62*, 416. (b) Mott, N. F. *Metal-insulator Transitions*; Taylor and Francis: London, 1990.

(4) Lahti, P. *Adv. Phys. Org. Chem.* **2011**, *45*, 93.

(5) (a) Kinoshita, M.; Turek, P.; Tamura, M.; Nozawa, K.; Shiomi, D.; Nakazawa, Y.; Ishikawa, M.; Takahashi, M.; Awaga, K.; Inabe, T.; Maruyama, Y. *Chem. Lett.* **1991**, 1225. (b) Tamura, M.; Nakazawa, Y.; Shiomi, D.; Nozawa, K.; Hosokoshi, Y.; Ishikawa, M.; Takahashi, M.; Kinoshita, M. *Chem. Phys. Lett.* **1991**, *186*, 401. (c) Chiarelli, R.; Novak, M. N.; Rassat, A.; Tholence, J. L. *Nature* **1993**, *363*, 147. (d) Alberola, A.; Less, R. J.; Pask, C. M.; Rawson, J. M.; Palacio, F.; Oliete, P.; Paulsen, C.; Yamaguchi, A.; Farley, R. D.; Murphy, D. M. *Angew. Chem., Int. Ed.* **2003**, *42*, 4782.

(6) Hubbard, J. *Proc. R. Soc. (London)* **1963**, *A276*, 238.

(7) In Hartree–Fock theory, for a 1D Hubbard chain, this condition becomes $W > (\pi/4)\,U$. See Whangbo, M. H. *J. Chem. Phys.* **1979**, *70*, 4763.

(8) (a) Haddon, R. C. *Nature* **1975**, *256*, 394. (b) Haddon, R. C. *Aust. J. Chem.* **1975**, *28*, 2333. (c) Haddon, R. C. *Aust. J. Chem.* **1975**, *28*, 2343.

(9) (a) Chi, X.; Itkis, M. E.; Patrick, B. O.; Barclay, T. M.; Reed, R. W.; Oakley, R. T.; Cordes, A. W.; Haddon, R. C. *J. Am. Chem. Soc.* **1999**, *121*, 10395. (b) Goto, K.; Kubo, T.; Yamamoto, K.; Nakasuji, K.; Sato, K.; Shiomi, D.; Takui, T.; Kubota, M.; Kobayashi, T.; Yakusi, K.; Ouyang, J. *J. Am. Chem. Soc.* **1999**, *121*, 1619. (c) Mandal, S. K.; Samanta, S.; Itkis, M. E.; Jensen, D. W.; Reed, R. W.; Oakley, R. T.; Tham, F. S.; Donnadieu, B.; Haddon, R. C. *J. Am. Chem. Soc.* **2006**, *128*, 1982. (d) Pal, S. K.; Itkis, M. E.; Tham, F. S.; Reed, R. W.; Oakley, R. T.; Haddon, R. C. *J. Am. Chem. Soc.* **2008**, *130*, 3942. (e) Morita, Y.; Suzuki, S.; Sato, K.; Takui, T. *Nature Chem.* **2011**, *3*, 197. (f) Nishida, S.; Kawai, J.; Moriguchi, M.; Ohba, T.; Haneda, N.; Fukui, K.; Fuyuhiro, A.; Shiomi, D.; Sato, K.; Takui, T.; Nakasuji, K.; Morita, Y. *Chem.—Eur. J.* **2013**, *19*, 11904.

(10) (a) Haddon, R. C.; Sarkar, A.; Pal, S. K.; Chi, X.; Itkis, M. E.; Tham, F. S. *J. Am. Chem. Soc.* **2008**, *130*, 13683. (b) Bag, P.; Itkis, M. E.; Pal, S. K.; Donnadieu, B.; Tham, F. S.; Park, H.; Schlueter, J. A.; Siegrist, T.; Haddon, R. C. *J. Am. Chem. Soc.* **2010**, *132*, 2684. (c) Huang, J.; Kertesz, M. *J. Am. Chem. Soc.* **2003**, *125*, 13334. (d) Huang, J.; Kertesz, M. *J. Am. Chem. Soc.* **2007**, *129*, 1634. (e) Bohlin, J.; Hansson, A.; Stafstrom, S. *Phys. Rev. B* **2006**, *74*, 155111. (f) Kubo, T.; Katada, Y.; Shimizu, A.; Hirao, Y.; Sato, K.; Takui, T.; Uruichi, M.; Yakushi, K.; Haddon, R. C. *J. Am. Chem. Soc.* **2011**, *133*, 14240. (g) Bag, P.; Pal, S. K.; Itkis, M. E.; Sarkar, S.; Tham, F. S.; Donnadieu, B.; Haddon, R. C. *J. Am. Chem. Soc.* **2013**, *135*, 12936.

(11) (a) Rawson, J. M.; Alberola, A.; Whalley, A. *J. Mater. Chem.* **2006**, *16*, 2560. (b) Hicks, R. G. In *Stable Radicals: Fundamentals and Applied Aspects of Odd-Electron Compounds*; Hicks, R. G., Ed.; John Wiley & Sons, Ltd., Wiltshire, 2010 pp 317–380. (c) Ratera, I.; Veciana, J. *Chem. Soc. Rev.* **2012**, *41*, 303. (d) Boeré, R. T.; Roemmele, T. L. *Comp. Inorg. Chem. II* **2013**, *1*, 375. (e) Rawson, J. M.; Hayward, J. J. *Handbook of Chalcogen Chemistry: New Perspectives in Sulfur, Selenium and Tellurium*; Devillanova, F., Du Mont, W.-W., Eds.; Royal Society of Chemistry: Cambridge, 2013; Vol 2; pp 69–98.

(12) Martín, N. *Chem. Commun.* **2013**, *49*, 7025.

(13) Cortizo-Lacalle, D.; Skabara, P. J.; Westgate, T. D. *Handbook of Chalcogen Chemistry: New Perspectives in Sulfur, Selenium and Tellurium*; Devillanova, F., Du Mont, W.-W., Eds.; Royal Society of Chemistry: Cambridge, 2013; Vol 2; pp 99–126.

(14) Cordes, A. W.; Haddon, R. C.; Oakley, R. T. *The Chemistry of Inorganic Ring Systems*, Steudel, R., Ed.: Elsevier, Amsterdam, 1992; Vol. *14*; pp 295–321.

(15) Peierls, R. C. *Quantum Theory of Solids*; Oxford University Press: London, 1955; p 108.

(16) Haynes, D. A. *CrystEngComm* **2011**, *13*, 4793.

(17) (a) Cordes, A. W.; Haddon, R. C.; Oakley, R. T. *Adv. Mater.* **1994**, *6*, 798. (b) Oakley, R. T. *Can. J. Chem.* **1993**, *71*, 1775.

(18) (a) Bryan, C. D.; Cordes, A. W.; Haddon, R. C.; Glarum, S. H.; Hicks, R. G.; Kennepohl, D. K.; MacKinnon, C. D.; Oakley, R. T.; Palstra, T. T. M.; Perel, A. S.; Schneemeyer, L. F.; Scott, S. R.; Waszczak, J. V. *J. Am. Chem. Soc.* **1994**, *116*, 1205. (b) Bryan, C. D.; Cordes, A. W.; Fleming, R. M.; George, N. A.; Glarum, S. H.; Haddon, R. C.; MacKinnon, C. D.; Oakley, R. T.; Palstra, T. T. M.; Perel, A. S. *J. Am. Chem. Soc.* **1995**, *117*, 6880. (c) Bryan, C. D.; Cordes, A. W.; Goddard, J. D.; Haddon, R. C.; Hicks, R. G.; MacKinnon, C. D.; Mawhinney, R. C.; Oakley, R. T.; Palstra, T. T. M.; Perel, A. S. *J. Am. Chem. Soc.* **1996**, *118*, 330.

(19) (a) Beer, L.; Brusso, J. L.; Cordes, A. W.; Haddon, R. C.; Itkis, M. E.; Kirschbaum, K.; MacGregor, D. S.; Oakley, R. T.; Pinkerton, A. A.; Reed, R. W. *J. Am. Chem. Soc.* **2002**, *124*, 9498. (b) Cordes, A. W.; Haddon, R. C.; Oakley, R. T. *Phosphorus, Sulfur, Silicon Relat. Elem.* **2004**, *179*, 673.

(20) The disproportionation energy ΔH_{disp} is the enthalpy change for the conversion of two gas-phase radicals R into a cation/anion pair, i.e., $2\,R \rightleftarrows R^+ + R^-$, and is equal to the difference between the IP and EA. The cell potential is defined here as the numerical difference between the half-wave potentials for the oxidation and reduction processes, that is, $|E_{cell} = E_{1/2}(ox) - E_{1/2}(red)|$.

(21) (a) Boeré, R. T.; Moock, K. H. *J. Am. Chem. Soc.* **1995**, *117*, 4755. (b) Boeré, R. T.; Roemmele, T. L. *Coord. Chem. Rev.* **2000**, *210*, 369. (c) Boeré, R. T.; Roemmele, T. L.; Yu, X. *Inorg. Chem.* **2011**, *50*, 5123. (d) Brusso, J. L.; Clements, O. P.; Haddon, R. C.; Itkis, M. E.; Leitch, A. A.; Oakley, R. T.; Reed, R. W.; Richardson, J. F. *J. Am. Chem. Soc.* **2004**, *126*, 8256.

(22) (a) Beer, L.; Britten, J. F.; Brusso, J. L.; Cordes, A. W.; Haddon, R. C.; Itkis, M. E.; MacGregor, D. S.; Oakley, R. T.; Reed, R. W.; Robertson, C. M. *J. Am. Chem. Soc.* **2003**, *125*, 14394. (b) Beer, L.; Britten, J. F.; Clements, O. P.; Haddon, R. C.; Itkis, M. E.; Matkovich, K. M.; Oakley, R. T.; Reed, R. W. *Chem. Mater.* **2004**, *16*, 1564.

(23) (a) Brusso, J. L.; Derakhshan, S.; Itkis, M. E.; Kleinke, H.; Haddon, R. C.; Oakley, R. T.; Reed, R. W.; Richardson, J. F.; Robertson, C. M.; Thompson, L. K. *Inorg. Chem.* **2006**, *45*, 10958. (b) Brusso, J. L.; Cvrkalj, K.; Leitch, A. A.; Oakley, R. T.; Reed, R. W.; Robertson, C. M. *J. Am. Chem. Soc.* **2006**, *128*, 15080.

(24) (a) Winter, S. M.; Datta, S.; Hill, S.; Oakley, R. T. *J. Am. Chem. Soc.* **2011**, *133*, 8126. (b) Pivtsov, A. V.; Kulik, L. V.; Makarov, A. Y.; Blockhuys, F. *Phys. Chem. Chem. Phys.* **2011**, *13*, 3873. (c) Winter, S. M.; Oakley, R. T.; Kovalev, A. E.; Hill, S. *Phys. Rev. B* **2012**, *85*, 094430.
(25) (a) Robertson, C. M.; Leitch, A. A.; Cvrkalj, K.; Reed, R. W.; Myles, D. J. T.; Dube, P. A.; Oakley, R. T. *J. Am. Chem. Soc.* **2008**, *130*, 8414. (b) Leitch, A. A.; Lekin, K.; Winter, S. M.; Downie, L. E.; Tsuruda, H.; Tse, J. S.; Mito, M.; Desgreniers, S.; Dube, P. A.; Zhang, S.; Liu, Q.; Jin, C.; Ohishi, Y.; Oakley, R. T. *J. Am. Chem. Soc.* **2011**, *133*, 6051.
(26) Leitch, A. A.; McKenzie, C. E.; Oakley, R. T.; Reed, R. W.; Richardson, J. F.; Sawyer, L. D. *Chem. Commun.* **2006**, 1088.
(27) Leitch, A. A.; Reed, R. W.; Robertson, C. M.; Britten, J. F.; Yu, X.; Secco, R. A.; Oakley, R. T. *J. Am. Chem. Soc.* **2007**, *129*, 7903.
(28) (a) Yu, X.; Mailman, A.; Dube, P. A.; Assoud, A.; Oakley, R. T. *Chem. Commun.* **2011**, *47*, 4655. (b) Yu, X.; Mailman, A.; Lekin, K.; Assoud, A.; Dube, P. A.; Oakley, R. T. *Cryst. Growth Des.* **2012**, *12*, 2485. (c) Yu, X.; Mailman, A.; Lekin, K.; Assoud, A.; Robertson, C. M.; Noll, B. C.; Campana, C. F.; Howard, J. A. K.; Dube, P. A.; Oakley, R. T. *J. Am. Chem. Soc.* **2012**, *134*, 2264. (d) Mailman, A.; Winter, S. M.; Yu, X.; Robertson, C. M.; Yong, W.; Tse, J. S.; Secco, R. A.; Liu, Z.; Dube, P. A.; Howard, J. A. K.; Oakley, R. T. *J. Am. Chem. Soc.* **2012**, *134*, 9886. (e) Wong, J. W. L.; Mailman, A.; Winter, S. M.; Robertson, C. M.; Holmberg, R. J.; Murugesu, M.; Dube, P. A.; Oakley, R. T. *Chem. Commun.* **2014**, *50*, 785.
(29) Desiraju, G. R. *Angew. Chem., Int. Ed. Engl.* **1995**, *34*, 2311.
(30) (a) Cozzolino, A. F.; Vargas-Baca, I.; Mansour, S.; Mahmoudkhani, A. H. *J. Am. Chem. Soc.* **2005**, *127*, 3184. (b) Cozzolino, F.; Vargas-Baca, I. *Cryst. Growth Des.* **2011**, *11*, 668.
(31) Haddon, R. C. *ChemPhysChem* **2012**, *13*, 3581.
(32) The resolution of the powder diffraction data for the β-phase was not sufficient to allow a Rietveld refinement.
(33) (a) Bondi, A. *J. Phys. Chem.* **1964**, *68*, 441. (b) Dance, I. *New J. Chem.* **2003**, *27*, 22.
(34) (a) Hobza, P.; Selzle, H. L.; Schlag, E. W. *J. Am. Chem. Soc.* **1994**, *116*, 3500. (b) Gavezzotti, A.; Desiraju, G. R. *Acta Crystallogr.* **1988**, *B44*, 427. (c) Bernstein, J.; Sarma, J. A. R. P.; Gavezzotti, A. *Chem. Phys. Lett.* **1990**, *174*, 361.
(35) Kuzmenko, A. B. *Rev. Sci. Instrum.* **2005**, *76*, 083108.
(36) (a) Georges, A.; Kotliar, G.; Krauth, W.; Rozenberg, M. J. *Rev. Mod. Phys.* **1996**, *68*, 13. (b) Basov, D. N.; Averitt, R. D.; Marel, D.; Dressel, M.; Haule, K. *Rev. Mod. Phys.* **2011**, *83*, 471.
(37) (a) Dumm, M.; Faltermeier, D.; Drichko, N.; Dressel, M.; Meziere, C.; Batail, P. *Phys. Rev. B* **2009**, *79*, 195106. (b) Faltermeier, D.; Barz, J.; Dumm, M.; Dressel, M.; Drichko, N.; Petrov, B.; Semkin, V.; Vlasova, R.; Meziere, C.; Batail, P. *Phys. Rev. B* **2007**, *76*, 165113.
(38) Merino, J.; Mackenzie, R. H. *Phys. Rev. B* **2000**, *61*, 7996.
(39) Ioffe, A. F.; Regel, A. R. *Prog. Semicond.* **1960**, *4*, 237.
(40) (a) Mayer, R.; Bleisch, S.; Domschke, G.; Tkáč, A.; Stăsko, A. *Org. Magn. Reson.* **1979**, *12*, 532. (b) Harrison, S. R.; Pilkington, R. S.; Sutcliffe, L. H. *J. Chem. Soc., Faraday Trans. 1* **1984**, *80*, 669. (c) Preston, K. F.; Sutcliffe, L. H. *Magn. Reson. Chem.* **1990**, *28*, 189. (d) Barclay, T. B.; Beer, L.; Cordes, A. W.; Oakley, R. T.; Preuss, K. E.; Taylor, N. J.; Reed, R. W. *Chem. Commun.* **1999**, 531.
(41) Lone pair mixing in **1a** is sufficiently strong that the unoccupied b_1 orbital is no longer the LUMO. It rises above two virtual levels of σ-symmetry.
(42) (a) Constantinides, C. P.; Koutentis, P. A.; Schatz, J. *J. Am. Chem. Soc.* **2004**, *126*, 16232. (b) Constantinides, C. P.; Ioannou, T. A.; Koutentis, P. A. *Polyhedron* **2013**, *64*, 172. (c) Langer, P.; Amiri, S.; Bodtke, A.; Saleh, N. N. R.; Weisz, K.; Görls, H.; Schreiner, P. R. *J. Org. Chem.* **2008**, *73*, 5048. (d) Amiri, S.; Schreiner, P. R. *J Phys. Chem. A* **2009**, *113*, 11750. (e) Barone, V.; Boilleau, C.; Cacelli, I.; Ferretti, A.; Monti, S.; Prampolini, G. *J. Chem. Theory Comput.* **2013**, *9*, 300. (f) Winter, S. M.; Roberts, R. J.; Mailman, A.; Cvrkalj, K.; Assoud, A.; Oakley, R. T. *Chem. Commun.* **2010**, *46*, 4496.
(43) (a) Noodleman, L. *J. Chem. Phys.* **1981**, *74*, 5737. (b) Noodleman, L.; Davidson, E. R. *Chem. Phys.* **1986**, *109*, 131. (c) Yamaguchi, K.; Jensen, F.; Dorigo, A.; Houk, K. N. *Chem. Phys. Lett.* **1988**, *149*, 537. (d) Nagao, H.; Nishino, M.; Shigeta, Y.; Soda, T.; Kitagawa, Y.; Onishi, T.; Yoshika, Y.; Yamaguchi, K. *Coord. Chem. Rev.* **2000**, *198*, 265.
(44) Cordes, A. W.; Goddard, J. D.; Oakley, R. T.; Westwood, N. P. C. *J. Am. Chem. Soc.* **1989**, *111*, 6147.
(45) (a) Borden, W. T.; Davidson, E. R. *J. Am. Chem. Soc.* **1977**, *99*, 4587. (b) Du, P.; Hrovat, D. A.; Borden, W. T.; Lahti, P. M.; Rossi, A. R.; Berson, J. A. *J. Am. Chem. Soc.* **1986**, *108*, 5072. (c) Du, P.; Borden, W. T. *J. Am. Chem. Soc.* **1987**, *109*, 930. (d) Bendikov, M.; Duong, H. M.; Starkey, K.; Houk, K. N.; Carter, E. A.; Wudl, F. *J. Am. Chem. Soc.* **2004**, *126*, 7416. (e) Bryan, C. D.; Cordes, A. W.; Goddard, J. D.; Haddon, R. C.; Hicks, R. G.; MacKinnon, C. D.; Mawhinney, R. C.; Oakley, R. T.; Palstra, T. T. M.; Perel, A. S. *J. Am. Chem. Soc.* **1996**, *118*, 330.
(46) Earlier band calculations on **3b−3d** (refs 28b−d) using the extended Hückel approximation gave rise to a reversal in the ordering of the SOMO and LUMO bands. Given the subtle energetic differences, correct orbital ordering near the Fermi level requires the use of SCF methods.
(47) (a) Kino, H.; Fukuyama, H. *J. Phys. Soc. Jpn.* **1996**, *65*, 2158. (b) McKenzie, R. H. *Comments Cond. Matt. Phys.* **1998**, *18*, 309. (c) Toyota, N.; Lang, M.; Muller, J. *Low-Dimensional Molecular Metals*; Springer: Berlin, 2007.
(48) Poteryaev, A. I.; Ferrero, M.; Georges, A.; Parcollet, O. *Phys. Rev. B* **2008**, *78*, 045115.
(49) (a) Goodenough, J. B. *Phys. Rev.* **1955**, *100*, 564. (b) Kahn. O. *Molecular Magnetism*; VCH Publishers, Inc.: New York, 1993, p 199.
(50) (a) Georges, A.; de' Medici, L.; Mravlje, J. *Annu. Rev. Condens. Matter Phys.* **2013**, *4*, 137. (b) de' Medici, L.; Mravlje, J.; Georges, A. *Phys. Rev. Lett.* **2011**, *107*, 256401.
(51) David, W. I. F.; Shankland, K.; van de Streek, J.; Pidcock, E.; Motherwell, W. D. S.; Cole, J. C. *J. Appl. Crystallogr.* **2006**, *39*, 910.
(52) Rietveld, H. M. *J. Appl. Crystallogr.* **1969**, *2*, 65.
(53) As a result of the rigid-body refinement model, standard deviations are not given for the bond and angle metrics for the structures obtained from powder diffraction data.
(54) Larson, A. C.; Von Dreele, R. B. *Report No. LA-UR-86-748*; Los Alamos National Laboratory: Los Alamos, NM, 1987.
(55) Le Bail, A.; Duroy, H.; Fourquet, J. L. *Mater. Res. Bull.* **1988**, *23*, 447.
(56) Secco, R. A.; Yong, W.; Officer, T. New 3000 Ton Multi-Anvil Press at the University of Western Ontario. *Abstract MR51A-02*. In Proceedings of American Geophysical Union Meeting, Cancun, Mexico, May 14−17, 2013; American Geophysical Union: Washington, D.C., 2013
(57) Frisch, M. J.; et al. *Gaussian 09*, revision A.02; Gaussian, Inc.: Wallingford, CT, 2009.
(58) Giannozzi, S.; et al. *J. Phys.:Condens. Matter* **2009**, *21*, 395502.